10-1-2014

The Spatial Cross-Correlation Method for Dispersive Surface Waves

Andrew P. Lamb
Boise State University

Kasper van Wijk
University of Auckland

Lee M. Liberty
Boise State University

T. Dylan Mikesell
Massachusetts Institute of Technology

Geophysical Journal International

Geophys. J. Int. (2014) **199,** 1–10
GJI Seismology

doi: 10.1093/gji/ggu237

The spatial cross-correlation method for dispersive surface waves

Andrew P. Lamb,[1,*] Kasper van Wijk,[2] Lee M. Liberty[1] and T. Dylan Mikesell[3]

[1]*Department of Geosciences, Boise State University, Boise, ID, USA. E-mail: andylamb@fastmail.fm*
[2]*Department of Physics, University of Auckland, Auckland, New Zealand*
[3]*Department of Earth, Atmospheric and Planetary Sciences, Massachusetts Institute of Technology, Cambridge, MA, USA*

Accepted 2014 June 17. Received 2014 May 25; in original form 2014 March 26

SUMMARY

Dispersive surface waves are routinely used to estimate the subsurface shear-wave velocity distribution, at all length scales. In the well-known Spatial Autocorrelation method, dispersion information is gained from the correlation of seismic noise signals recorded on the vertical (or radial) components. We demonstrate practical advantages of including the cross-correlation between radial and vertical components of the wavefield in a spatial cross-correlation method. The addition of cross-correlation information increases the resolution and robustness of the phase velocity dispersion information, as demonstrated in numerical simulations and a near-surface field study with active seismic sources, where our method confirms the presence of a fault-zone conduit in a geothermal field.

Key words: Interferometry; Hydrothermal systems; Surface waves and free oscillations; North America.

1 INTRODUCTION

The dispersion of surface waves is commonly used to characterize the lithosphere (e.g. Knopoff 1972; Bensen *et al.* 2007), as well as the near-surface (e.g. Nazarian *et al.* 1983; Park *et al.* 1999; Socco & Strobbia 2004). In a medium with a vertically heterogeneous velocity distribution, the surface wave phase velocity is frequency dependent. Retrieving these dispersive properties allows us to invert for (shear) wave velocity as a function of depth.

Dispersion information from the correlation of surface waves in Aki's SPatial AutoCorrelation method (SPAC, Aki 1957) was more recently exploited (e.g. Ekström *et al.* 2009; Stephenson *et al.* 2009). Tsai & Moschetti (2010) established the equivalence between SPAC and the time-domain versions since made popular as 'seismic interferometry' (e.g. Wapenaar & Fokkema 2006). In related work, the REfraction MIcrotremor method (REMI Louie 2001) maps the near-surface velocity distribution using the dispersion observed in cross-correlations of signals from a combination of ambient noise and human activity. Until recently, analyses have been limited to the vertical or the radial components of the wavefield. However, van Wijk *et al.* (2011) explored cross-correlations of the off-diagonal components (radial and vertical) of the Green's tensor and found these to be more robust in the presence of uneven Rayleigh wave illumination on the receivers. This approach was followed by a formal extension of the SPAC method to the complete Green's tensor by Haney *et al.* (2012). In addition to enhancement of the surface wave dispersion information, these additional cross-correlations can be used to enhance the body wave arrivals (van Wijk *et al.* 2010; Takagi *et al.* 2014)

Here we explore extending SPAC to include SPatial cross-correlation (SPaX) of radial and vertical components. In SPaX, we correlate all combinations of the vertical and radial wavefield components to extract more robust estimates of the dispersive Rayleigh wave. The additional components increase accuracy and resolution of the surface wave dispersion information. Numerical modelling of the full wavefield illustrates the advantages, and we demonstrate this with an example using active-source seismic data from a geothermal field site at Mount Princeton Hot Springs, Colorado.

2 THEORY

Consider a Rayleigh plane wave travelling with a phase velocity c along the surface in the positive x-direction of a homogeneous 2-D elastic half-space. For a source at position x_s along the surface, the displacement wavefield recorded at surface position x is $U_z(x_s, x, t)$, where subscript z represents the vertical component and t is time. At another surface location $x' > x$, we record $U_z(x_s, x', t)$. These two wavefields are identical to each other, except for the time delay between the signals that is $(x' - x)/c$. It is therefore quite intuitive that the cross-correlation of the two wavefields from an impulsive source at x_s is

$$U_z(x^s, x', t) \otimes U_z(x^s, x, t) = \delta\,(t - r/c)\,, \tag{1}$$

where $\otimes$ denotes the cross-correlation and $r = |x' - x|$ is the interreceiver distance. In principle, if the two receivers are bounded by a source on each side, the correlation of the wavefields

*Now at: U.S. Geological Survey, 345 Middlefield Rd, Menlo Park, CA 94025, USA.

results in the causal and acausal component of the Green's function [$\delta(t - r/c)$ and $\delta(t + r/c)$].

The SPAC method explores this same principle, but in the frequency domain. The real part of the Fourier transform of the retarded Dirac delta function is

$$\phi_{zz}(r, \omega) = \Re[\mathcal{F}(\delta(t - r/c))] = \cos(\omega r/c), \tag{2}$$

where ϕ_{zz} was referred to by Aki (1957) as the SPAC coefficient for the vertical component correlation. By cross-correlating all four combinations of vertical $U_z(x, t)$ and radial $U_x(x, t)$ wavefield recordings, we create the four SPaX coefficients

$$\phi(r, \omega) = \begin{bmatrix} \phi_{zz} & \phi_{zx} \\ \phi_{xz} & \phi_{xx} \end{bmatrix}, \tag{3}$$

where ϕ_{zz} and ϕ_{xx} are the SPAC coefficients, and ϕ_{zx} and ϕ_{xz} are the spatial cross-correlation coefficients. Eq. (26) of Haney *et al.* (2012) summarizes the derivation of all four components of the frequency domain Rayleigh wave Green's tensor for 1-D wave propagation

$$\phi(r, \omega) = P(\omega) \begin{bmatrix} \cos(\omega r/c) & -R \sin(|\omega| r/c) \\ R \sin(|\omega| r/c) & R^2 \cos(\omega r/c) \end{bmatrix}, \tag{4}$$

where R is the ratio of the horizontal-to-vertical displacement of the Rayleigh waves and $P(\omega)$ is the power spectrum of the Rayleigh waves.

Ekström *et al.* (2009) use the roots of the real part of Aki's SPAC coefficient [$\Re e(\phi_{zz}(\omega)) = 0$] to estimate the dispersion relationship of Rayleigh waves. For the spatial autocorrelation terms in eq. (4), this means that $\omega r/c = n\pi/2$ and we find the phase velocity relationship

$$c_{zz}(\omega_n) = c_{xx}(\omega_n) = \frac{\omega_n r}{n\pi/2}, \tag{5}$$

where ω_n represents the nth root of the cosine function. Here, we add the information about the phase velocity estimates by correlating all combinations of the wavefields, including the cross-correlations of vertical and radial components:

$$c_{zx}(\omega_n) = c_{xz}(\omega_n) = \frac{\omega_n r}{n\pi}. \tag{6}$$

In the following, we illustrate some of the strengths and outstanding challenges of the SPaX technique with numerical examples, before ending with a near-surface field example from a vibroseis survey.

3 SPATIAL CROSS-CORRELATION IN A HOMOGENEOUS SLAB

The previous section outlined the extraction of the Rayleigh-wave information. In reality, interference from other wave modes contaminates the Rayleigh-wave information. In a finite half-space, for example, body waves reflect from the bottom of the medium. In this section, we use elastic-wave numerical modelling in such a slab to investigate degradation of surface wave dispersion curves caused by interfering body waves.

The parameters of the numerical experiment for a slab are displayed in Fig. 1. The slab is 50 m thick with *P*- and *S*-wave velocities of 900 and 500 m s^{-1}, respectively. The Rayleigh-wave velocity is 462 m s^{-1}. We simulate wave propagation for 11 source positions (black stars) having distances to the first receiver (inverted open triangles) ranging from 10 to 110 m at a 10 m interval. The Ricker source wavelet has a dominant frequency of 30 Hz. The surface receiver spacing is 2 m and the sample rate is 2000 Hz. We model the radial and vertical components of the wavefield using SPECFEM2D

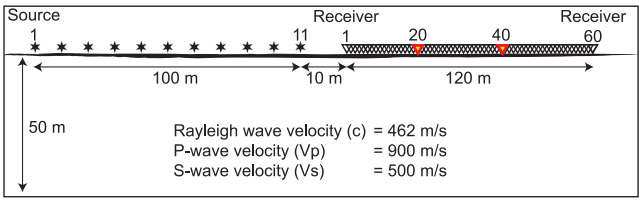

Figure 1. A schematic of the 50-m-thick slab model with sources and receivers at the surface.

for 60 receiver positions. SPECFEM2D is a high-order variational numerical algorithm (Priolo *et al.* 1994; Faccioli *et al.* 1997) and is widely used in applications ranging from seismology (Komatitsch & Vilotte 1998; Komatitsch & Tromp 1999, 2002; Komatitsch *et al.* 2002) to ultrasonics (van Wijk *et al.* 2004).

3.1 Vertical component wavefield correlations

The vertical component of the wavefield for all 60 receivers from source 6 is presented in the left-hand panel of Fig. 2. The Rayleigh waves—characterized by a linear moveout—have the largest amplitudes, but body-wave reflections intersect the Rayleigh waves. These body waves complicate Rayleigh wave signal isolation that is required for many inversion schemes. In the SPAC method, averaging long recording times improves the distribution of source locations, minimizing the effects of interfering body waves. Analogous to the SPAC method, considering active sources at varying locations with respect to the receiver locations leads to the same result. The middle panel of Fig. 2 is the correlation of the vertical component of the wavefields at receivers 20 and 40, for sources 1–10. While the correlation between Rayleigh waves is stationary ($t \sim 0.08$ s), the correlated energy associated with body-wave reflections varies in arrival time from source to source. Hence, summing the cross-correlated wavefields for all sources results in constructive interference of Rayleigh waves and destructive interference of all other wave modes. The top trace (*sum*) shows the average of the 10 lower traces. This method exploits the correlation of sources at so-called stationary phase points (Snieder 2004; van Wijk 2006). Next, the cross-correlation of all receivers with receiver 20—summed over all sources—leads to the virtual shot record shown in the right-hand panel of Fig. 2.

In the virtual shot record, the body waves have almost disappeared and a strong Rayleigh wave is present. To demonstrate how multiple source summation improves the SPAC coefficients, we show $\phi_{zz}(r, \omega)$ in Fig. 3, where $r = 40$ m as receiver 20 is correlated with receiver 40. As observed in the time domain (Fig. 2, middle), summing wavefield correlations from multiple sources stabilizes the estimate of ϕ_{zz}. The differences between the single source correlation and the summed version highlights the influence of body-wave interference, which can lead to biased phase velocity estimates. Note that the band-limited nature of our numerical modelling decreases the signals below 10 Hz (and above 70 Hz). We discuss the implications of this in a later section, but first we will consider the advantage of adding spatial cross-correlations to the autocorrelation results.

3.2 Multicomponent wavefield correlations

Analogous to the *zz* component of the SPAC method, in Fig. 4 we plot the spatial autocorrelation (*xx* and *zz* components) and cross-correlation (*xz* and *zx* components) coefficients for receivers 20 and 40 after summing over shots 1 to 10. These components behave as the harmonic functions predicted by eq. (4), and we

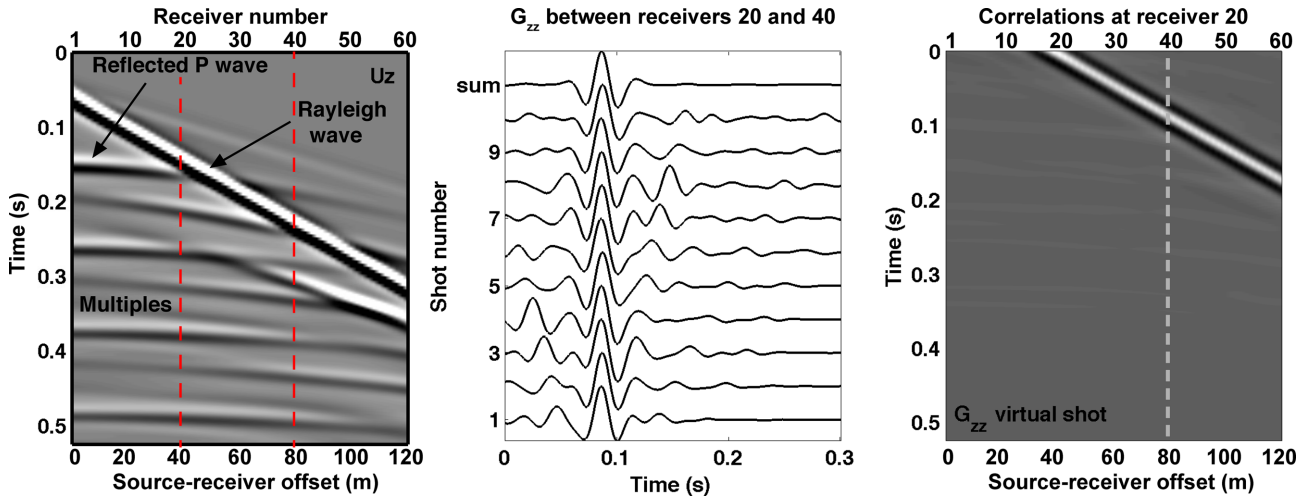

Figure 2. Left-hand panel: the vertical component of the wavefield in a slab from single shot, U_z at source position 6. Middle panel: the correlation functions between receivers 20 and 40 for sources 1 to 10, G_{zz}. The top trace shows the results of summing these 10 shots. Right-hand panel: the virtual shot record for all 60 receivers, with the virtual source at receiver 20.

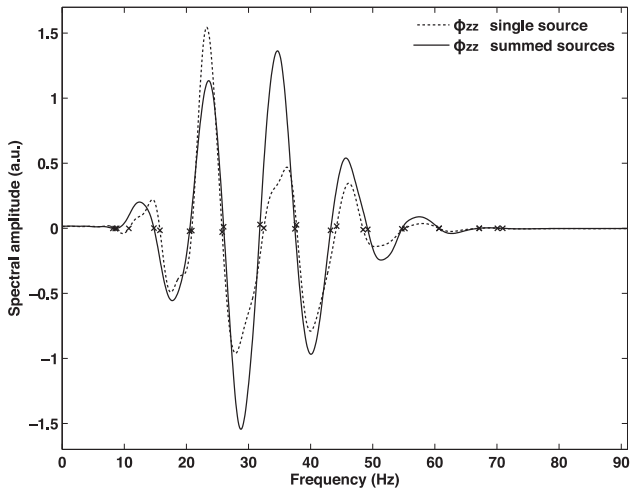

Figure 3. The real part of the Fourier transform of the cross-correlation of the vertical components of receivers 20 and 40 for a single source at source position 6 and for the sum of 10 sources. Each 'x' marks a zero crossing—or root—of this function.

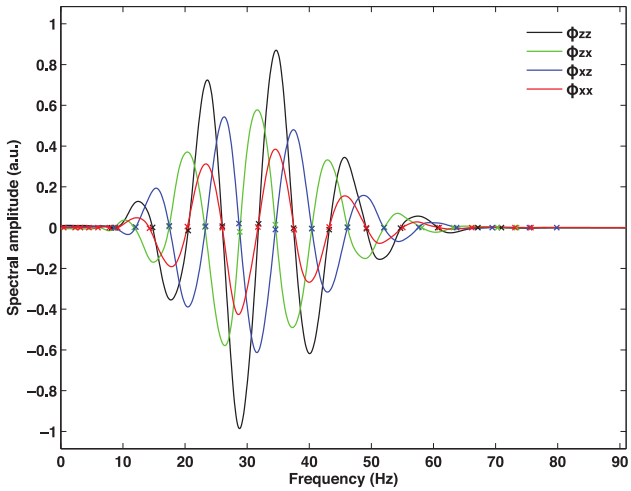

Figure 4. SPaX coefficients ϕ_{zz}, ϕ_{zx}, ϕ_{xz} and ϕ_{xx} from the 10 summed shots.

note the $\pi/2$ phase shift between spatial autocorrelation and cross-correlation coefficients, as well as the antisymmetry between the cross-correlation coefficients.

From the roots—or zero-crossings—of the harmonic functions in Fig. 4, we estimate the phase-velocity curves shown in Fig. 5 (bottom panel). The top panel is the phase-velocity estimate from a single source, whereas the bottom panel contains the estimates after source summation. The substantial difference between ϕ_{zz} and the other three SPAC coefficients is due to a mis-identified root of ϕ_{zz}, as a result of body wave interference. Estimates of the phase velocity from the other terms are centred about the correct Rayleigh velocity of 462 m s^{-1} with a standard deviation of 15 m s^{-1}.

The curves from the summed sources in the bottom panel of Fig. 5 show significantly less variability. The summation over sources results in the correct root n identification, due to the suppression of body-wave interference. Estimation of the phase velocity is more difficult at low frequency, for two reasons. First, in our slab model the finite thickness affects the Rayleigh waves at long wavelengths. Second, the source wavelet has limited power at the lowest frequencies. The latter is also the reason why it is common practice that the first root is not used in field applications of the SPAC method (Ekström *et al.* 2009; Tsai & Moschetti 2010).

To quantify the improvements of using the sum of 10 sources for all four SPaX coefficients, Fig. 6 contains the mean (solid diamond) and standard deviation of the Rayleigh-wave velocity estimate for each source position, and for the sum of all sources (open diamond). At certain individual source positions, the errors due to body-wave interference with the Rayleigh-wave signal is large. The standard deviation for the summed result is reduced considerably, demonstrating the improved velocity estimation using all possible Rayleigh-wave information.

3.3 Missing roots

When signals lack energy in the low-end of the frequency spectrum, it is entirely possible we fail to identify the first zero-crossing of the harmonic functions of eqs (5) and (6). If unidentified, this will bias the entire estimate of the surface-wave dispersion curve. To accurately estimate dispersion curves we need to estimate how many roots of the harmonic functions are missing. In our estimation, we

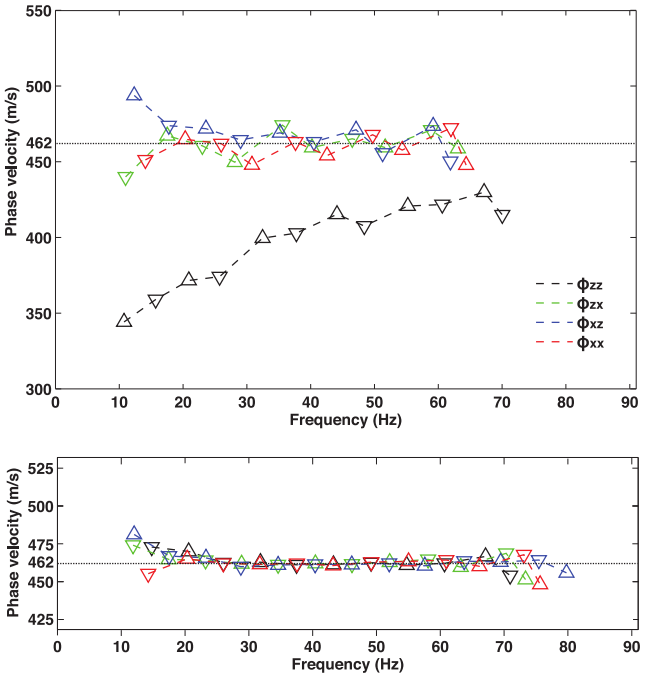

Figure 5. The roots of the real part of the Fourier transform of the cross-correlations between receivers 20 and 40 for all four components for a single shot at source position 6 (top panel) and for 10 summed shots (bottom panel). The top and bottom panels have the same vertical scale and colour relationship between ϕ terms. The upward and downward pointing triangle symbols indicate whether the slope of the zero-crossing is negative or positive respectively.

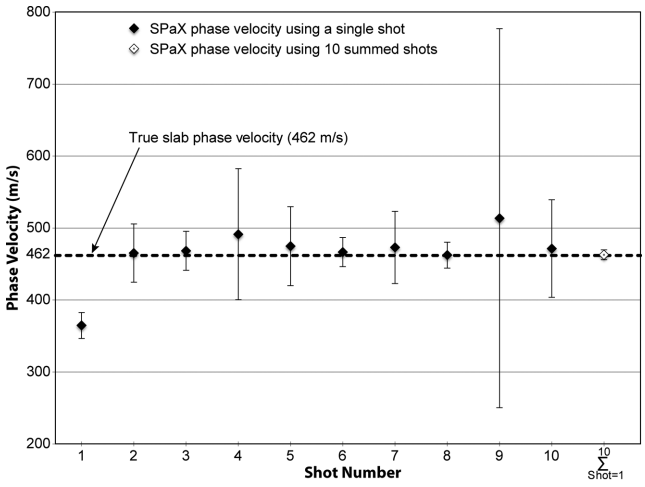

Figure 6. The mean phase velocity from all four SPaX coefficients with the corresponding standard deviation. Each point has been averaged over all frequencies before averaging the individual SPaX components. Solid diamonds represent single source locations, while the open diamond shows the results after summing over 10 sources.

follow a similar procedure to Ekström *et al.* (2009) and calculate a series of phase velocity dispersion curves c^m that are based on adaptations of eqs (5) and (6). For the autocorrelation coefficients we write

$$c^m_{zz,xx}(\omega_n) = \frac{\omega_n r}{(n+m)\pi/2}, \tag{7}$$

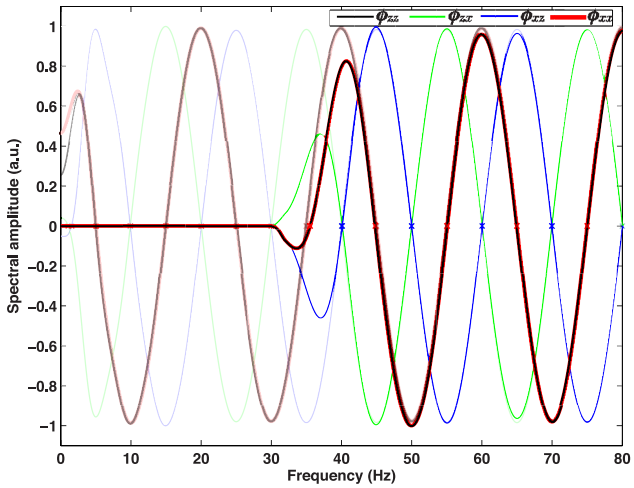

Figure 7. The semitransparent (0–150 Hz) and full-colour (30–150 Hz) SPaX coefficients from a homogeneous half-space model.

and for the cross-correlation coefficients we write

$$c^m_{zx,xz}(\omega_n) = \frac{\omega_n r}{(n+m)\pi}, \tag{8}$$

where m represents the number of missed roots incremented in multiples of 2.

The SPaX method uses all four correlation coefficients to estimate the missed roots and thereby improves our estimation of the dispersion curves. In practice, we estimate missed zero crossings by knowing that: (1) the roots of the off-diagonal and diagonal terms follow a sine and cosine function, respectively and (2) the phase velocities must fall within certain physical limits constrained by prior information (Ekström *et al.* 2009). The dispersion curves for the SPaX coefficients are jointly interpreted to minimize error.

To demonstrate our multicomponent approach we again turn to numerical modelling. Instead of a slab model, we use to a homogeneous half-space model so that body reflections from the bottom of the model do not exist. The model has a Rayleigh-wave phase velocity of $c = 500$ m s^{-1}. We place two receivers at the surface, separated by a distance r. In this experiment, we use a single source location, but repeat the experiment. The first experiment uses a sinusoidal chirp sweep from 30 to 150 Hz and the second use the same sweep but from 0 to 150 Hz. In this way, we illustrate the influence of the missing roots and compare with the correct data.

For each source, we cross-correlate all receiver combinations to compute the SPaX coefficients (Fig. 7). We see that for ϕ_{zz} and ϕ_{xx} in the partial-band case (30–150 Hz), there are three missing zero crossings while for ϕ_{zx} and ϕ_{xz} there are four missing zero crossings. The complete-band case (0–150 Hz) shows all of the zero crossings—indicated by the partially transparent data.

With $m = 3$ in eq. (7) for the diagonal terms and $m = 4$ in eq. (8) for the off-diagonal terms of the SPaX method, we estimate the correct phase-velocity curves. To see the influence of using the incorrect m value, we plot a variety of dispersion curves in Fig. 8.

Fig. 7 shows that the slope of the SPaX coefficients near the zero crossings vary between components. In this example, the slope is positive for the first crossing of ϕ_{xz} and negative for the other three coefficients ϕ_{zz}, ϕ_{zx} and ϕ_{xx}. When m follows an odd number series (e.g. 1, 3, 5, . . .), this means the first available zero crossing in our data occurs at a slope of ϕ that is opposite in direction to the slope of ϕ at the first missed root.

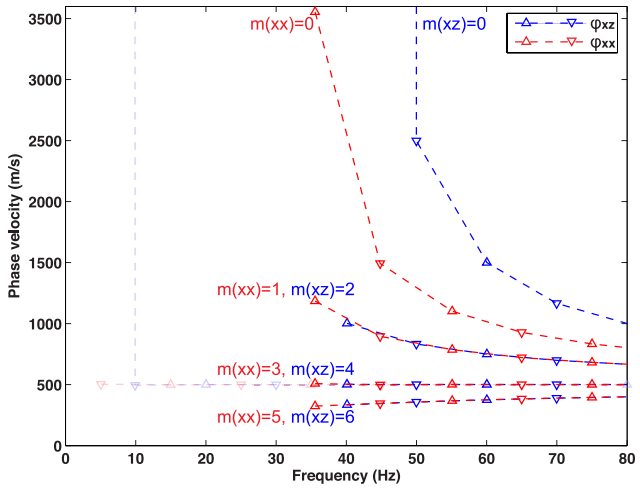

Figure 8. Estimates of phase velocity versus frequency in the homogeneous slab, from a sweep between 30 and 150 Hz. Because we are missing information from 0 to 30 Hz, there are a number of possible dispersion curves that explain the data. In this case, the band-limited data of the numerical experiment resulted in SPaX coefficients that lacked three roots in the diagonal terms and four in the cross-terms. The transparent curve is the estimate of phase velocity when we add the low-frequency information in our numerical simulation.

Estimating m was relatively straightforward in the absence of dispersion, where the zero crossings are evenly spaced. To understand the effects of dispersion on the estimation of the dispersion curve when lacking low-frequency signals, we investigate a dispersive numerical model in the next section.

4 SPATIAL CROSS-CORRELATION IN DISPERSIVE MEDIA

In Fig. 9 the Rayleigh wave velocity changes from 480 to 600 m s^{-1} at a depth of 12 m. Again we use SPECFEM2D to simulate wavefields and sum correlations from 12 source positions with offsets to the first receiver ranging from 10 to 120 m, at 10 m increments. An approximation to the Dirac delta source provides broad-band signals, and the recorded wavefields are low-pass (150 Hz) filtered. Fig 9 shows two receivers with a spacing $r = 40$.

The shot records and related correlation function estimates for this example are presented in Lamb (2013). The correlation coefficients for a receiver separation of $r = 40$ m are shown in Fig. 10. The black-solid line is the result of summing all four SPaX coefficients, after the cross-correlation terms ϕ_{xz} and ϕ_{zx} have been phase rotated by 90°. The phase-velocity dispersion curves calculated from these correlation coefficients are plotted in Fig. 11. The dispersion curve of the combination of the four SPaX coefficients matches the correct phase velocities best.

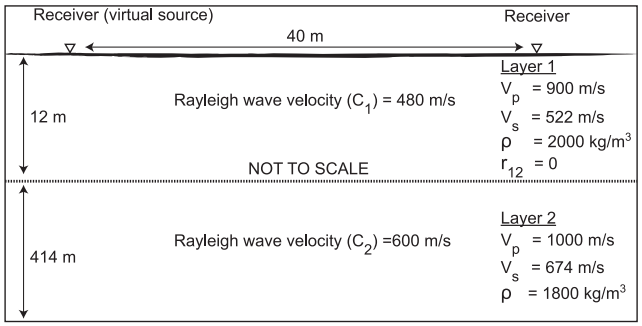

Figure 9. A schematic of the two-layer numerical model. Because of the differing velocity in each layer, the Rayleigh wave velocity is dispersive. The depth of the model is large, so that it effectively acts as a half-space.

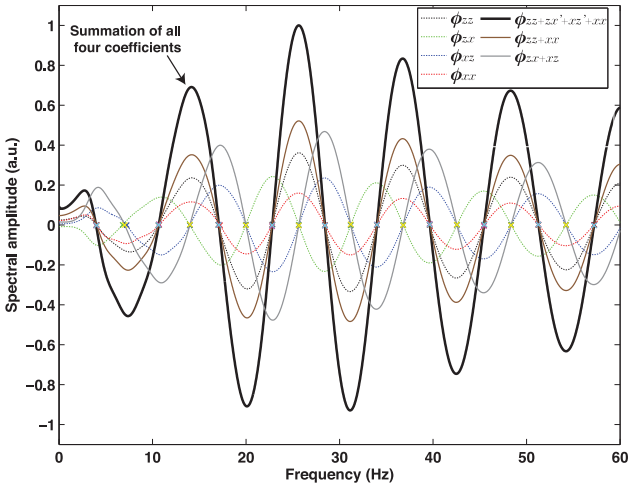

Figure 10. The individual and combined SPaX coefficients after summing the 12 shots for a receiver separation of 40 m. The coloured 'x' symbols are the estimated zero crossings for all components.

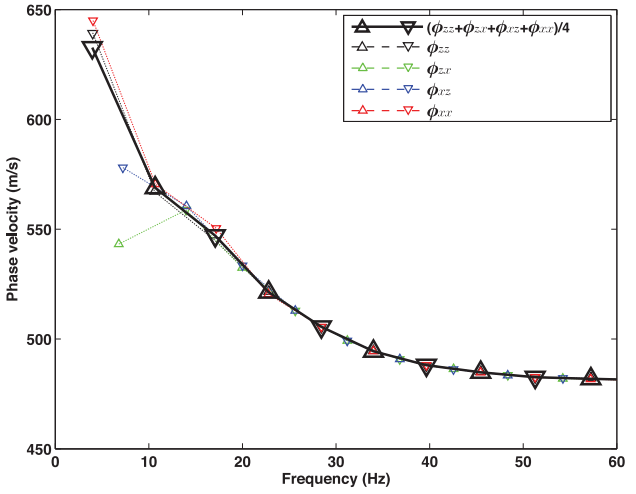

Figure 11. Phase-velocity dispersion curves from all four individual SPaX coefficients between receivers separated by 40 m. The solid-black line shows the result of averaging all four SPaX coefficients to calculate phase velocity c.

The curves in Fig. 11 show that the phase velocity decreases with increasing frequency from ∼600 to 480 m s^{-1}. The slower layer of the model is predominantly sampled by the higher frequency Rayleigh waves—48 Hz and above where the maximum Rayleigh wavelength is 12 m. Furthermore, these frequencies propagate at a slow enough velocity that the body waves do not interfere in time and space. Thus, there is a negligible difference in the dispersion curves above 48 Hz. In contrast, below 48 Hz the Rayleigh-wave phase velocity increases and body waves interfere. Thus, there is some variability (e.g. at 18 Hz) in the dispersion curves. Below 12 Hz the dispersion curves diverge more strongly, because the physical dimensions of the numerical model are less than the Rayleigh wavelengths at these low frequencies.

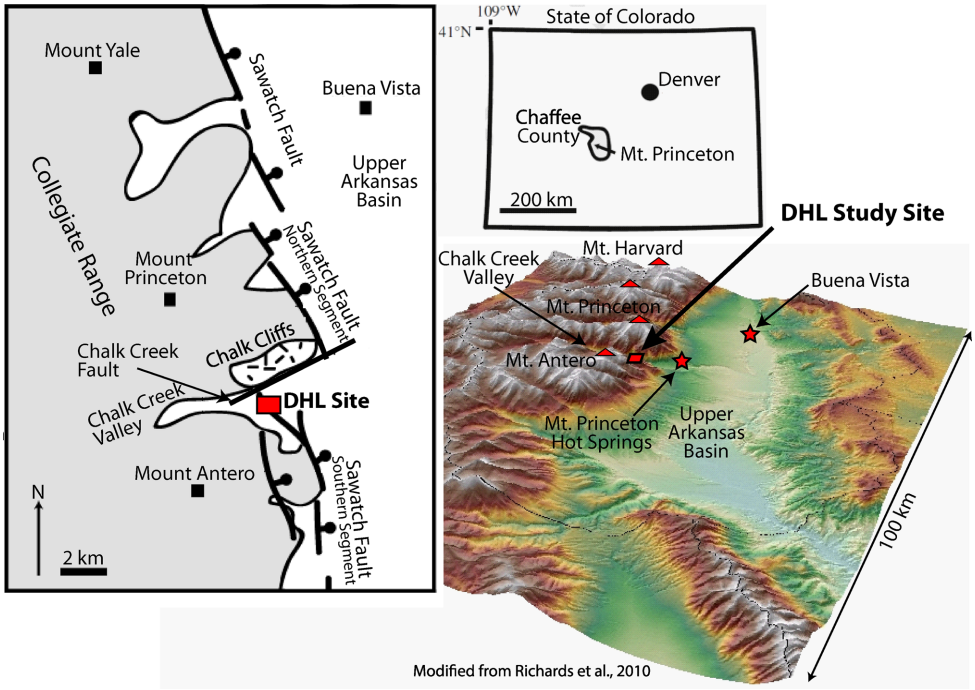

Figure 12. Top right-hand panel: Colorado state map showing the approximate locations of Chaffee County, Mount Princeton, and Denver. Bottom right-hand panel: a topographic map of the Upper Arkansas basin in Chaffee County superimposed with the Dead Horse Lake (DHL) study site. Left-hand panel: location of faults mapped along the Sawatch Range according to work by Scott *et al.* (1975), Colman *et al.* (1985) and Miller (1999).

5 A FIELD APPLICATION

The Upper Arkansas Valley in the Rocky Mountains of central Colorado is the northernmost extensional basin of the Rio Grande Rift (Fig. 12). The valley is a half-graben bordered to the east and west by the Mosquito and Sawatch Ranges, respectively (McCalpin & Shannon 2005). The Sawatch range-front normal fault strikes north-northwest along the eastern margin of the Collegiate Peaks and is characterized by a right-lateral offset between the Mount Princeton batholith and Mount Antero. This offset in basin bounding faults is accommodated by a northeast–southwest dextral strike-slip transfer fault (Richards *et al.* 2010) and coincides with an area of hydrogeothermal activity including Mount Princeton Hot Springs. This transfer fault is here termed the 'Chalk Creek fault' due to its alignment with the Chalk Creek valley. A 250 m high erosional scarp, called the Chalk Cliffs, lies along the northern boundary of this valley. The cliffs are comprised of geothermally altered quartz monzonite (Miller 1999). These cliffs coincide with the Chalk Creek fault, whose intersection with the Sawatch range-front normal fault results in a significant pathway for upwelling geothermal waters.

The Dead Horse lake (DHL) site in Chalk Creek Valley (Fig. 12) coincides with a north-south trending boundary (dash–dotted line in Fig. 13) between hot- and cold-water wells to the west and east, respectively. The site is characterized by 10–50 m deep glacial, fluvial and alluvial deposits overlying a quartz monzonite and granite basement. Dead Horse lake is dry for most of the year.

We acquired and processed a series of geophysical data at DHL to image the subsurface and identify potential geothermal pathways. The geophysical methods that we used included a gravity survey, a ground magnetic survey, a vertical seismic profile (VSP), a seismic refraction tomography survey, and a seismic surface wave survey. The seismic data included a nine component data set which we used for applying the SPAC and SPaX surface wave methods. The detailed results for these surveys and data analysis are presented in Lamb (2013).

We conducted a gravity survey using a Scintrex CG-5 gravimeter on a 50 m grid; the data have been corrected for drift, latitude, free-air, Bouguer and terrain. The reduced gravity data are shown in the colour overlay in Fig. 13. The gravity data suggest an eastward dip in the underlying bedrock with a difference of approximately 4 mGal across the survey area (~600 m) in the west–east direction. We also conducted a VSP survey in the 168 m deep MG-1 borehole (Fig. 13) to constrain the seismic interval velocities and to determine the depth to competent granite (Lamb 2013).

The location of the active seismic experiment is indicated in Fig. 13—coincident dotted and solid black lines. We acquired multicomponent seismic data using a 2720 kg Industrial Vehicles T-15000 vibroseis source along a dirt track in an east–northeasterly direction. The vibroseis truck can be configured as a *P*- and *S*-wave source. The seismic line extends from station 1 to 236, and the station interval is 2 m, giving a total line length of 472 m. The vibroseis data were recorded using a 120 channel Geometrics recording system and 10-Hz three component geophones. The vibroseis source was a 14 second linear sweep from 30 to 300 Hz.

We carried out a 2-D refraction tomography analysis using the correlated vertical (*Uz*) component of the seismic data. A commercial refraction tomography software code called RayFract (Intelligent Resources Inc.) was used. The vibroseis data were correlated using a synthetic sweep trace, time shifted to account for time-shifts in the clipped pilot trace.

The interpreted refraction tomography velocity model presented in Fig. 14 has an rms error of 1.3 per cent between the forward-modelled and observed first arrival picks. This interpretation was constrained by the MG-1 well log and VSP results presented in Lamb (2013). Our interpretation is that the saturated sediments and altered quartz monzonite interfaces to the east of MG-1 appear to have little variability in elevation. There is a decrease in the velocity

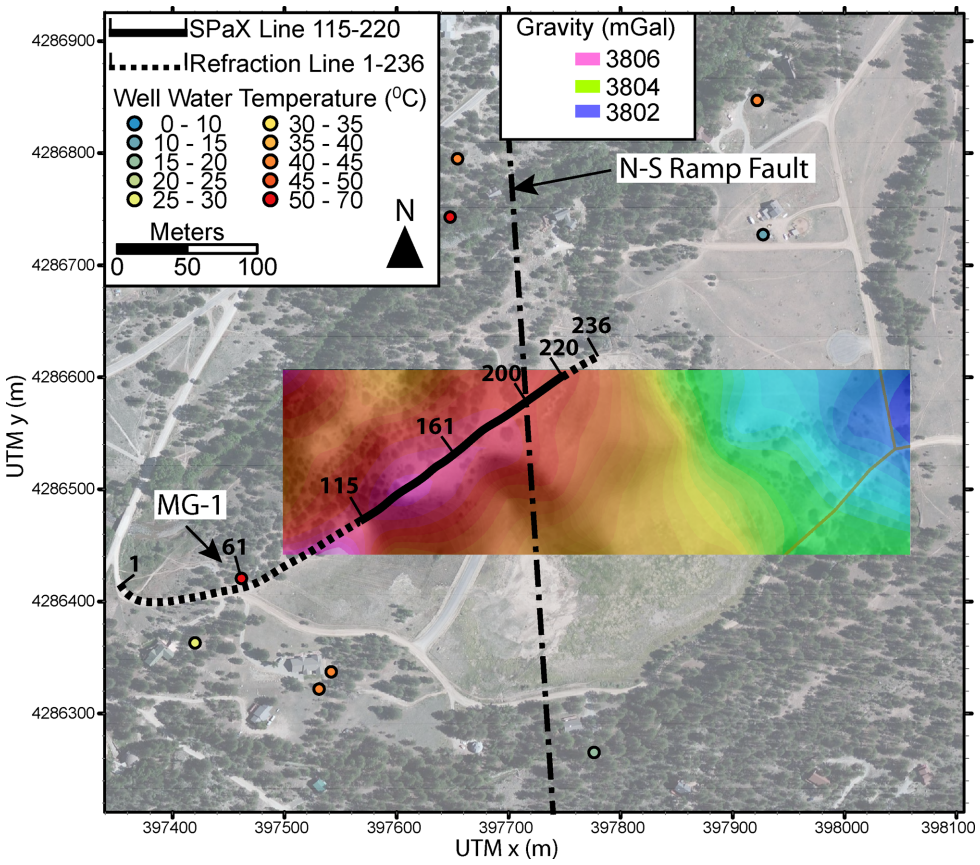

Figure 13. The Dead Horse Lake (DHL) study site showing water wells and their temperatures, the location of the seismic line, and overlain with the reduced gravity data. The well labelled MG-1 was used to conduct a 168 m deep vertical seismic profile for which the results are presented in Lamb (2013).

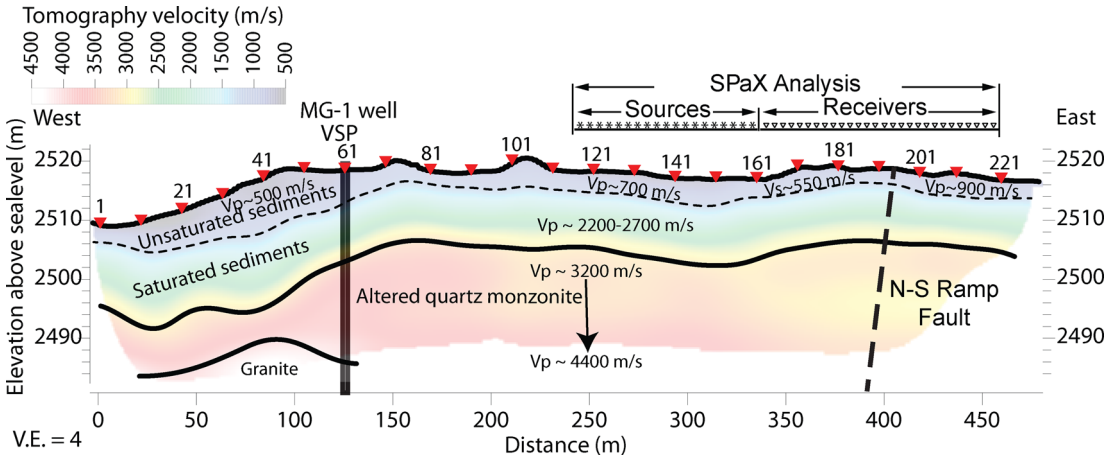

Figure 14. A geological interpretation of the SPaX result and refraction tomography velocities constrained by the MG-1 well (Lamb 2013).

of the quartz monzonite to the east and this may be a result of geothermal alteration and more fracturing of the rock. The velocity profile shows a region of over 4000 m s^{-1} at an elevation of 2486 m near MG-1. This is also observed in the VSP data (Lamb 2013). The absence of this velocity to the east of the refraction velocity profile along with slower refraction events observed in shot gathers (Lamb 2013) further suggests a deepening of the competent granite to the east. Estimating the depth of this >4000 m s^{-1} layer is difficult to the east. However, through observation of the slower quartz monzonite velocities and negative gravity gradient, we interpret this faster layer to be in the elevation range of 2480–2420 m, which corresponds to a depth range of 40–100 m. The lower elevation of 2420 m could be facilitated by a north–south offset ramp fault (east-side down) which is interpreted to cross in this region. This fault is shown traversing the DHL site in the left-hand panel of Fig. 12 and its location is based upon work by Miller (1999). This north–south ramp fault may also be responsible for the gravity gradient.

Nine component data were acquired between stations 115 and 236. We apply the SPaX analysis to the stations between 115 and 220 (solid black line in Fig. 13) where the acquisition geometry is

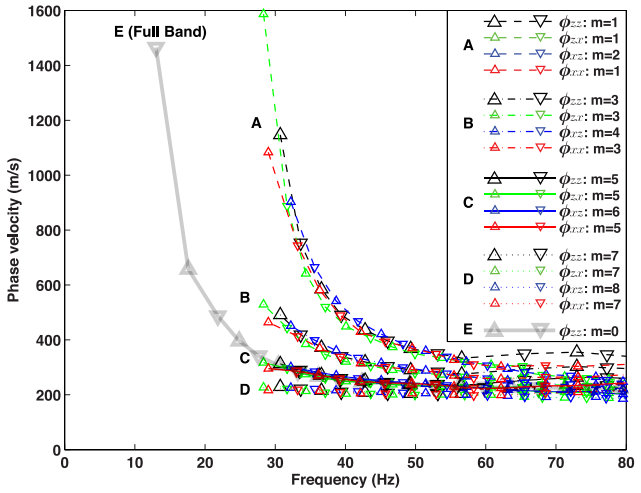

Figure 15. Phase-velocity dispersion curves for field data where $r = 30$ m. The semitransparent and full-colour dispersion curves are for full-band (numerical) and partial-band (field) data, respectively. The full-band curve E is from a numerical calculation, with a model based on all the prior geological and geophysical information (Lamb 2013). Because the vibroseis sweep did not cover the frequency range 0–30 Hz, we estimate that $m_{zz,zx,xx} = 5$ and $m_{xz} = 6$. This is receiver pair 116 and 131.

more or less linear. It is common that the sweep trace is not perfectly known (or recorded), so that correlating the data with the estimated sweep can introduce errors. Fortunately, one of the advantages of the SPaX method is that we can use the uncorrelated vibroseis data. Lamb (2013) provided examples of the benefits of using uncorrelated sweep data by comparing the SPaX results from correlated and uncorrelated seismic data when the sweep trace is an incomplete representation of the vibroseis input signal. The examples demonstrate that using correlated versus uncorrelated sweeps can cause up to a 10 per cent variation in phase-velocity dispersion curve estimates for zero crossings near 30 Hz. The field data results presented in the remainder of this paper are all based upon uncorrelated vibroseis data.

5.1 Dispersion curves from spatial cross-correlation

The shot records and correlation coefficients for this field example are presented in Lamb (2013), which also describes a numerical model based on the suite of geological and geophysical data gathered at the site. These include seismic refraction tomography, gravity and magnetic surveys, and a VSP in a well at the western end of our receiver line. With this numerical model we can estimate the number of missed zero crossings (m) in the DHL SPaX coefficients.

Fig. 15 shows the phase-velocity dispersion curves at a receiver separation of 30 m in the virtual shot gathers. Curves A through D represent dispersion curves for different numbers of missed zero crossings (m). The zero crossings are selected such that the slope of the first zero crossing matches the theoretical slope of the cosine function (down) and sine function (up). The numerical dispersion curve (grey line) from the 32-layer model is shown to help determine the number of missed zero crossings in the field data; the numerical data are full-band (i.e. 0–300 Hz). Because the vibroseis sweep did not cover the frequency range 0–30 Hz, the numerical data suggests that the number of missed zero crossings is $m_{zz,zx,xx} = 5$ and $m_{xz} = 6$, respectively. With the number of missed zero crossings estimated, we proceed to address the variability in dispersion curves related to the lateral geologic heterogeneity along the DHL seismic line.

5.2 Lateral variations

To develop an understanding of the lateral variability along the DHL seismic line, we plot the SPaX coefficient gathers in Fig. 16. We show two cases—(lower left-hand panel) (ϕ_{xx}) and (lower right-hand panel) ($\phi_{zz} + \phi_{xz} + \phi_{zx} + \phi_{xx}$). The lower left-hand panel in Fig. 16 shows $\phi_{xx}(r = 30, \omega)$ for receivers 168–213. The traces are plotted at the midpoint between the two receivers and the red dashed line follows the 7th zero crossing for each curve. This line provides a qualitative measure of lateral variability, because it does not represent velocity at a specific depth. Eqs (5) and (6) help to intuitively understand these variations, where the frequency (ω_n) and phase velocity (c_n) are linearly proportional to each other. A trend in the red line towards lower frequency near midpoint 187 represents a lower seismic wave speed locally. The blue dashed line in the upper panel shows the corresponding phase velocity at the 7th zero crossing. The phase velocity generally decreases from midpoint 187–212 by approximately 60 m s^{-1}.

The bottom right-hand panel in Fig. 16 shows the combined SPaX coefficients for the same receivers as in the bottom left-hand plot. Comparison of the SPAC and SPaX gathers in the bottom panels demonstrates the improvement in signal coherency from combining all four components. In particular, the stations from 168 to 194 show less variability in the SPaX coefficients. Furthermore, inclusion of all components of the Green's tensor provided information at stations where the vertical component of the wavefield was not recorded due to geophone failure. Examples include midpoints 170, 184, 191 and 205. There is also an improvement in the signal-to-noise ratio for the zero crossings in the frequency range of 41–47 Hz and midpoints 168–184.

The gravity anomaly of Fig. 13 is interpreted as a N–S ramp fault to accommodate two parts of the Sawatch normal fault that are offset across the Chalk Creek valley. The seismic tomography model of Fig. 14 is inherently smooth, but the eastward reduction in velocity from 3500 to 3000 m s^{-1} at an elevation of 2495 m is likely the fault's imprint on the smooth seismic refraction velocity model. Furthermore, the SPaX coefficients as presented in Fig. 16 demonstrate the methods ability to identify potential lateral lithology variations that may be further evidence for the N–S ramp fault. The loss in signal coherence east of midpoint 190 may be aided by geometric spreading of the seismic energy, but given prior information from independent geophysical data, we attribute at least part of the coherency loss to the N–S ramp fault. The east side of this ramp faults hanging wall will have more deformed and disturbed sedimentary units that can cause reduced coherency in seismic data. This is a possible explanation for the SPaX coefficient gathers losing coherency on the 7th zero crossing picks, as this is a function of the geologic heterogeneity east of the N–S ramp fault.

The midpoint gather of SPaX coefficient curves of Fig. 16 is a useful tool to quickly assess spatial changes in lateral velocity. Visualization with different receiver separations r can be used to control the number of SPaX-coefficient gather zero crossings in a specific frequency range. For instance, increasing r will cause more sign changes in the SPaX coefficients for the receiver pair, with a corresponding increase in the number of zero crossings. Even though a larger r adds a higher density of zero crossings in the SPaX coefficients for a given frequency range, this can mask lateral heterogeneity because the wavefield is averaged over more of the structure with increasing r. Therefore, increases in r make it more difficult to determine the correct number of missing zero crossings.

The joint geologic interpretation of all of our geophysical techniques for the Dead Horse lake field site fits a four-layer model that,

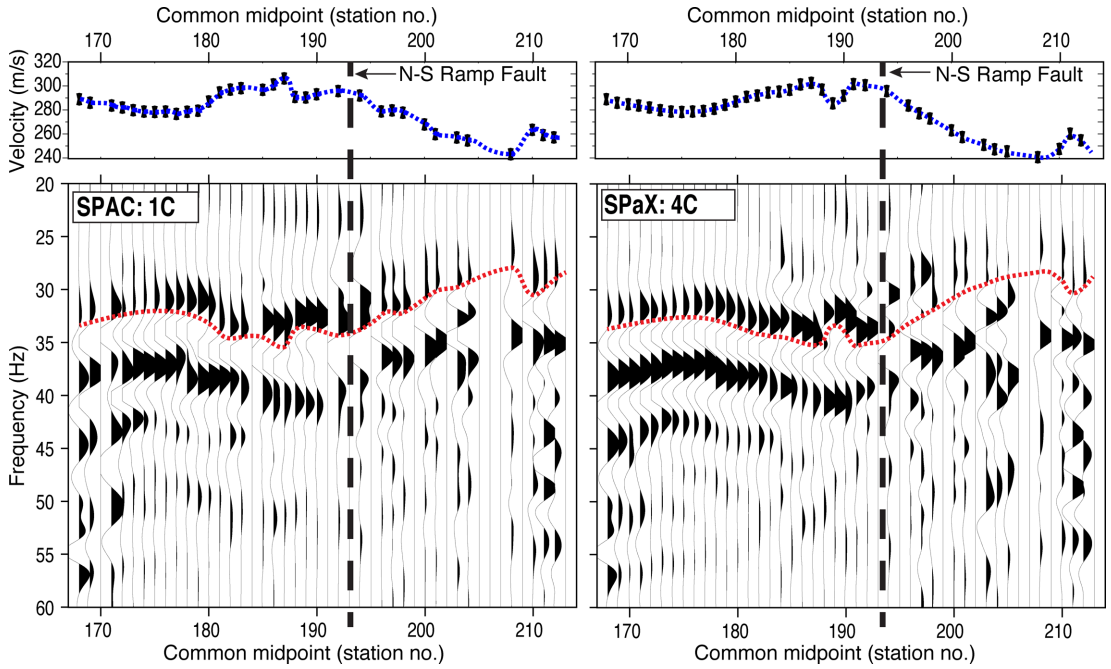

Figure 16. Lower left-hand panel: a gather of SPAC coefficient traces for $\phi_{xx}(r = 30, \omega)$ for the field data from station 168 to 213. The dashed red line shows the 7th zero crossings. The phase velocity corresponding to the 7th zero crossings is shown in the top panel and indicates laterally changing velocity. Bottom right-hand panel: a gather of the average correlation coefficients. Top right-hand panel: the phase velocity corresponding to 7th zero crossing of the combined SPaX coefficients.

with increasing depth, is composed of unsaturated sediments, saturated sediments, altered quartz monzonite and competent granite. The interpretation of these layers, along with further detail about all the analyses performed, are described in Lamb (2013). The seismic and gravity data show evidence for the N–S ramp fault (Miller 1999) between Mount Antero and Mount Princeton near station 200 on the seismic line. The SPaX results provide further evidence for the N–S ramp fault commencing from midpoint 200 eastwards. This fault may well be a pathway for hot geothermal waters, but requires further geophysical investigations along its strike through the Chalk Creek valley.

6 CONCLUSION

The extension of the SPAC method to include cross-correlations of the wavefield (SPaX) results in dispersion curves that are more robust and of a higher resolution. The increased robustness is a function of the added independent data, while the resolution improvements stem from estimating phase velocities at additional frequencies in SPaX. As in the SPAC method, prior information is needed for the SPaX method when the lowest frequencies are not present in the data.

In the field, there are practical advantages to include cross-correlations of the radial and vertical components of the wavefield to characterize near-surface velocities. In the case of vibroseis sources, there is no need for (potentially damaging) correlations with the sweep, and SPaX coefficients can be used directly to identify lateral variations in the subsurface.

ACKNOWLEDGEMENTS

All data used in this study are freely available upon request from the authors. Funding for this research was provided by the Department of Energy award G018195 and the National Science Foundation award EAR-1142154. Additional funding for the vibroseis was provided by the NSF. We would like to thank the local community and land owners for giving us access to their properties. We also thank Chaffee County, the SEG Foundation, ION Geophysical, field camp students and other local stakeholders for their support. The seismic and gravity data were acquired from 2008 to 2010 as part of the geophysical field camp attended by students from the Colorado School of Mines, Boise State University and Imperial College London. Other individuals who contributed to this work include Mike Batzle, Thomas Blum, Justin Ball, Seth Haines, André Revil, Kyle Richards and Fred Henderson.

REFERENCES

Aki, K., 1957. Space and time spectra of stationary stochastic waves, with special reference to microtremors, *Bull. Earthq. Res. Inst.,* **35,** 415–456.

Bensen, G.D., Ritzwoller, M.H., Barmin, M.P., Levshin, A.L., Lin, F., Moschetti, M.P., Shapiro, N.M. & Yang, Y., 2007. Processing seismic ambient noise data to obtain reliable broad-band surface wave dispersion measurements, *Geophys. J. Int.,* **169**(3), 1239–1260.

Colman, S.M., McCalpin, J.P., Ostenaa, J.P. & Kirkham, D.A., 1985. Map showing upper cenozoic rocks and deposits and quaternary faults, Rio Grande rift, south-central Colorado, *U.S. Geological Survey Miscellaneous Investigations Map I-1594,* U.S. Geological Survey, Denver, CO.

Ekström, G., Abers, G.A. & Webb, S.C., 2009. Determination of surface-wave phase velocities across USArray from noise and Aki's spectral formulation, *Geophys. Res. Lett.,* **36,** L18301, doi:10.1029/2009GL039131.

Faccioli, E., Maggio, F., Paolucci, R. & Quarteroni, A., 1997. 2D and 3D elastic wave propagation by a pseudo-spectral domain decomposition method, *J. Seismol.,* **1,** 237–251.

Haney, M.M., Mikesell, T.D., van Wijk, K. & Nakahara, H., 2012. Extension of the spatial autocorrelation (SPAC) method to mixed-component correlations of surface waves, *Geophys. J. Int.,* **191**(1), 189–206.

Knopoff, L., 1972. Observation and inversion of surface-wave dispersion, *Tectonophysics,* **13**(1), 497–519.

Komatitsch, D. & Tromp, J., 1999. Introduction to the spectral-element method for 3-D seismic wave propagation, *Geophys. J. Int.,* **139,** 806–822.

Komatitsch, D. & Tromp, J., 2002. Spectral-element simulations of global seismic wave propagation—I. Validation, *Geophys. J. Int.,* **150,** 390–412.

Komatitsch, D. & Vilotte, J.P., 1998. The spectral-element method: an efficient tool to simulate the seismic response of 2D and 3D geological structures, *Bull. seism. Soc. Am.,* **88,** 368–392.

Komatitsch, D., Ritsema, J. & Tromp, J., 2002. The spectral-element method, Beowulf computing, and global seismology, *Science,* **298,** 1737–1742.

Lamb, A.P., 2013. Geophysical investigations of the seattle fault zone in western washington and a geothermal system at mount princeton, Colorado, *PhD thesis,* Boise State University.

Louie, J.N., 2001. Faster, better: shear-wave velocity to 100 meters depth from refraction microtremor arrays, *Bull. seism. soc. Am.,* **91**(2), 347–364.

McCalpin, J.P. & Shannon, J.R., 2005. Geologic map of the Buena Vista west quadrangle, Chaffee County, Colorado, *Open-File Report 05-8, Colorado Geological Survey,* Department of Natural Resources, Denver, CO.

Miller, M.G., 1999. Active breaching of a geometric segment boundary in the Sawatch range normal fault, Colorado, USA, *J. Struct. Geol.,* **21**(7), 769–776.

Nazarian, S.K., Stokoe II, H. & Hudson, W.R., 1983. Use of spectral-analysis-of-surface-waves method for determination of moduli and thickness of pavement systems, Tech. Rep. 930, Transportation Research Record.

Park, C.B., Miller, R.D. & Xia, J., 1999. Multichannel analysis of surface waves, *Geophysics,* **64**(3), 800–808.

Priolo, E., Carcione, J.M. & Seriani, G., 1994. Numerical simulations of interface waves by high-order spectral modeling techniques, *J. acoust. Soc. Am.,* **95,** 681–693.

Richards, K., Revil, A., Jardani, A., Henderson, F., Batzle, M. & Haas, A., 2010. Pattern of shallow ground water flow at Mount Princeton Hot Springs, Colorado, using geoelectrical methods, *J. Volc. Geotherm. Res.,* **198**(1–2), 217–232.

Scott, G.R., Van Alstine, R.E. & Sharp, W.N., 1975. Geologic map of the Poncha Springs Quadrangle, Chaffee County, Colorado, *U.S. Geological Survey Miscellaneous Field Studies Map MF-658,* U.S. Geological Survey, Denver, CO.

Snieder, R., 2004. Extracting the Green's function from the correlation of coda waves: a derivation based on stationary phase, *Phys. Rev. E,* **69**(4), doi:10.1103/PhysRevE.69.046610.

Socco, L.V. & Strobbia, C., 2004. Surface-wave method for near-surface characterization: a tutorial, *Near Surf. Geophys.,* **2**(4), 165–185.

Stephenson, W., Hartzell, S., Frankel, A., Asten, M., Carver, D. & Kim, W., 2009. Site characterization for urban seismic hazards in Lower Manhattan, New York city, from microtremor array analysis, *Geophys. Res. Lett.,* **36,** L03301, doi:10.1029/2008GL036444.

Takagi, R., Nakahara, H., Kono, T. & Okada, T., 2014. Separating body and rayleigh waves with cross terms of the cross-correlation tensor of ambient noise, *J. geophys. Res.: Solid Earth,* **119**(3), 2005–2018.

Tsai, V.C. & Moschetti, M.P., 2010. An explicit relationship between time-domain noise correlation and spatial autocorrelation (SPAC) results, *Geophys. J. Int.,* **182**(1), 454–460.

van Wijk, K., 2006. On estimating the impulse response between receivers in a controlled ultrasonic experiment, *Geophysics,* **71**(4), SI79–SI84.

van Wijk, K., Komatitsch, D., Scales, J.A. & Tromp, J., 2004. Analysis of strong scattering at the micro-scale, *J. acoust. Soc. Am.,* **115,** 1006–1101.

van Wijk, K., Mikesell, D., Blum, T., Haney, M. & Calvert, A., 2010. Surface wave isolation with the interferometric Green's tensor, in *Proceedings of the SEG Technical Program Expanded Abstracts,* Denver, CO, pp. 3996–4000.

van Wijk, K., Mikesell, T.D., Schulte-Pelkum, V. & Stachnik, J., 2011. Estimating the Rayleigh-wave impulse response between seismic stations with the cross terms of the Green's tensor, *Geophys. Res. Lett.,* **38,** L16301, doi:10.1029/2011GL047442.

Wapenaar, K. & Fokkema, J., 2006. Green's function representations for seismic interferometry, *Geophysics,* **71**(4), SI33–SI46.